Diamond formation mechanism in chemical vapor deposition

Meiyan Jiang[a,1], Chengke Chen[a,1] , Ping Wang[a], Difeng Guo[a], Sijia Han[a], Xiao Li[a], Shaohua Lu[a] , and Xiaojun Hu[a,2]

It is a key challenge to prepare large-area diamonds by using the methods of high-pressure high-temperature and normal chemical vapor deposition (CVD). The formation mechanism of thermodynamically metastable diamond compared to graphite in low-pressure CVD possibly implies a distinctive way to synthesize large-area diamonds, while it is an intriguing problem due to the limitation of in situ characterization in this complex growth environment. Here, we design a series of short-term growth on the margins of cauliflower-like nanocrystalline diamond particles, allowing us to clearly observe the diamond formation process. The results show that vertical graphene sheets and nanocrystalline diamonds alternatively appear, in which vertical graphene sheets evolve into long ribbons and graphite needles, and they finally transform into diamonds. A transition process from graphite (200) to diamond (110) verifies the transformation, and Ta atoms from hot filaments are found to atomically disperse in the films. First principle calculations confirm that Ta-added H- or O-terminated bilayer graphene spontaneously transforms into diamond. This reveals that in the H, O, and Ta complex atmosphere of the CVD environment, diamond is formed by phase transformation from graphite. This subverts the general knowledge that graphite is etched by hydrogen and sp^3 carbon species pile up to form diamond and supplies a way to prepare large-area diamonds based on large-sized graphite under normal pressure. This also provides an angle to understand the growth mechanism of materials with sp^2 and sp^3 electronic configurations.

nanocrystalline diamond films | chemical vapor deposition | graphite-diamond phase transformation

Diamond possesses excellent physical properties, such as high hardness, wide band, high thermal conductivity, negative electronic affinity, and strong corrosion resistance, so it has a wide range of applications in electronic devices used in high-temperature high-frequency field emission devices, electrochemical electrodes, and so on. It is also considered a multifunctional material and attracts much attention. However, it is very difficult to prepare large-area diamonds, which is a barrier to their application. Researchers have developed various methods, including high-pressure high-temperature (HPHT) and chemical vapor deposition (CVD) to prepare single crystals, microcrystallines, and nanocrystalline diamonds (1–5). Expensive equipment and rare large diamond seeds are required to prepare large-area diamonds by using the HPHT and CVD methods, respectively. It is noticed that thermodynamically metastable diamond compared to graphite grows in low-pressure CVD. Its formation mechanism possibly implies a distinctive way to synthesize large-area diamonds, while it is an intriguing problem due to the limitation of in situ characterization in this complex growth environment.

Eversole (6) developed a CVD method to prepare diamonds under low pressures, and Matsumoto et al. (7) made a breakthrough in CVD technology. Since then, various activation methods for CVD diamond have been successfully developed (8), and the growing process of diamond basically includes nucleation and growth. A diamond nucleation site was responsible for epitaxial growth of diamond on silicon (9), and a model for diamond nucleation by energetic species in CVD was proposed (10). Using high-resolution electron energy loss spectroscopy, researchers found that CH_x radicals were related to the growth of diamond (111)/(100) planes (11, 12). Based on optical emission spectroscopy data (13, 14), C_2 was first considered a dominant species for ultrananocrystalline diamond (UNCD) growth, while ground-state C_2 was undetectable in a $He/CH_4/H_2$ plasma and was too low in concentration in the $Ar/CH_4/H_2$ plasma to account for the growth rate of UNCD (15). Another study found remarkably high concentrations of C_2 and atomic hydrogen in an $Ar/CH_4/H_2$ microwave plasma (16). It was also supposed that H atoms etched amorphous and sp^2 carbon quicker than diamond, and sp^3 contained carbon active groups as units piled up at the active vacancy positions to form diamond (11, 12, 17–24). The above results clearly suggest that there are debates existing in the growth mechanism of CVD diamond due

Significance

Artificial diamond plays a vital role in the manufacturing industry, jewelry, and future photoelectronic devices, but it is a key challenge to prepare the required large-area diamonds. A distinctive way to solve this problem possibly hides in the undiscovered formation mechanism of thermodynamically metastable diamond compared to graphite in low-pressure chemical vapor deposition. We design a series of short-term growth on the margins of cauliflower-like nanocrystalline diamond particles and find that diamond is formed by the transformation from graphite, not by the piling up of sp^3 carbon. Atomically dispersed Ta atoms let the transition spontaneously occur. This subverts the general knowledge and supplies a way to prepare large-area diamonds based on large-sized graphite under normal pressure.

to the lack of in situ characterization technology. It is still difficult to answer the following questions: should the nondiamond species truly be dregs eroded away by H and is there any relationship among the nondiamond species and diamond phases in the CVD process? These are key points to understand the diamond formation mechanism in CVD that will inspire preparation methods for diamond and provide comprehension for the growth of other materials with sp^2 and sp^3 electronic configurations.

Here, we performed a series of short-term growths on cauliflower-like separated particle-formed (SPF) films (25) to produce nanometer-scale surfaces (*SI Appendix*, Fig. S1), directly observed by high-resolution transmission electron microscopy (HRTEM) without extra treatments, preventing damage produced by traditional TEM sample preparation, and allowing us to observe the real growth process of nanocrystalline diamond (NCD) films. We find that diamond is formed by a phase transition from graphite.

Fig. 1*A* reveals a typical cauliflower-like morphology of particles on the SPF film (defined as 0-s sample). A large number of vertical-growing sheets formed as the growth time increased to 30 s (Fig. 1*B*, called 30-s sample), and they became larger at 60 s

(Fig. 1*C*, called 60-s sample). Nevertheless, these sheets disappear in 90 s (Fig. 1*D*, called 90-s sample), exhibiting bald cauliflower-like particles again. For 120 s (Fig. 1*E*, called 120-s sample), the sheets still disappear, while they appear and become larger again in 150 s (Fig. 1*F*, called 150-s sample) and 180 s (Fig. 1*G*, called 180-s sample), respectively. At 210 s, some sheets turned into nanoparticles marked by red arrows in Fig. 1*H*, suggesting that the sheets disappeared as growth proceeded. These results indicate that vertical-growing sheets and bald cauliflower-like particles alternately appear with two circles of 0 to 90 s and 120 to 210 s.

Visible Raman spectra (Fig. 1 *I* and *I*-1) reveal the composition evolution. The 0-s sample exhibits the typical Raman characterics of NCD films (26). For samples 30-s and 60-s, only four peaks at D band (1,350 cm^{-1}), G band (1,580 cm^{-1}), strong D' (1,620 cm^{-1}), and D+D' peaks (2,700 cm^{-1}) are related to graphene and its edge defects (27, 28), respectively, indicating that the vertical-growing sheets observed in the scanning electron microscopy (SEM) graphs (Fig. 1 *B*, *C*, *F*, and *G*) are graphene, called vertical-growing graphene sheets (VGs). After 90 s and 120 s of growth, typical characteristics of NCD appear again with the enlarged full width half maximum (FWHM) of the G peaks, and graphene-related peaks at 2,700
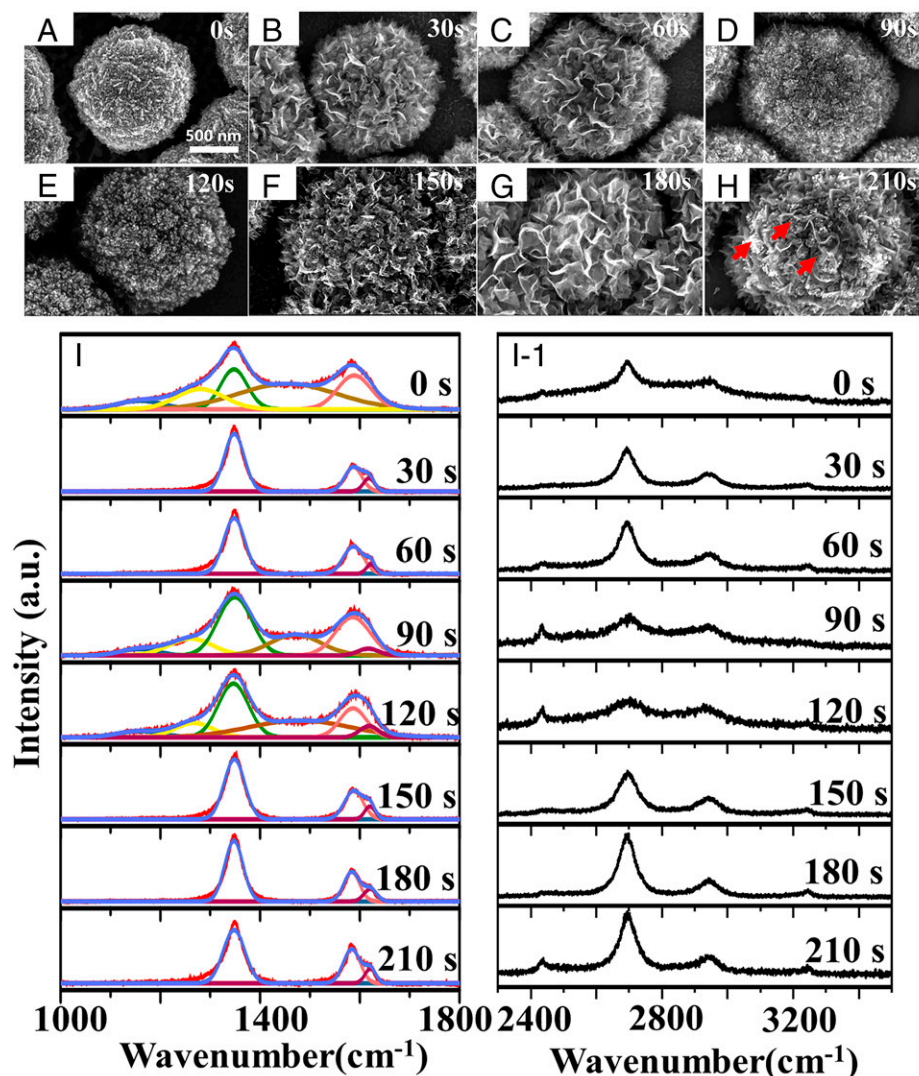
Fig. 1. FESEM images for samples growing using (*A*) 0 s, (*B*) 30 s, (*C*) 60 s, (*D*) 90 s, (*E*) 120 s, (*F*) 150 s, (*G*) 180 s, and (*H*) 210 s during the second growth process at 1,800 W. The red arrows in (*H*) are used to mark the nanoparticles. The Raman spectra of the 1,000–1,800 cm^{-1} range after Gauss fitting (*I*) and 2,300–3,500 cm^{-1} range (*I*-1) are shown. The red line is raw curve and the other colored lines are fitted curves in (*I*).

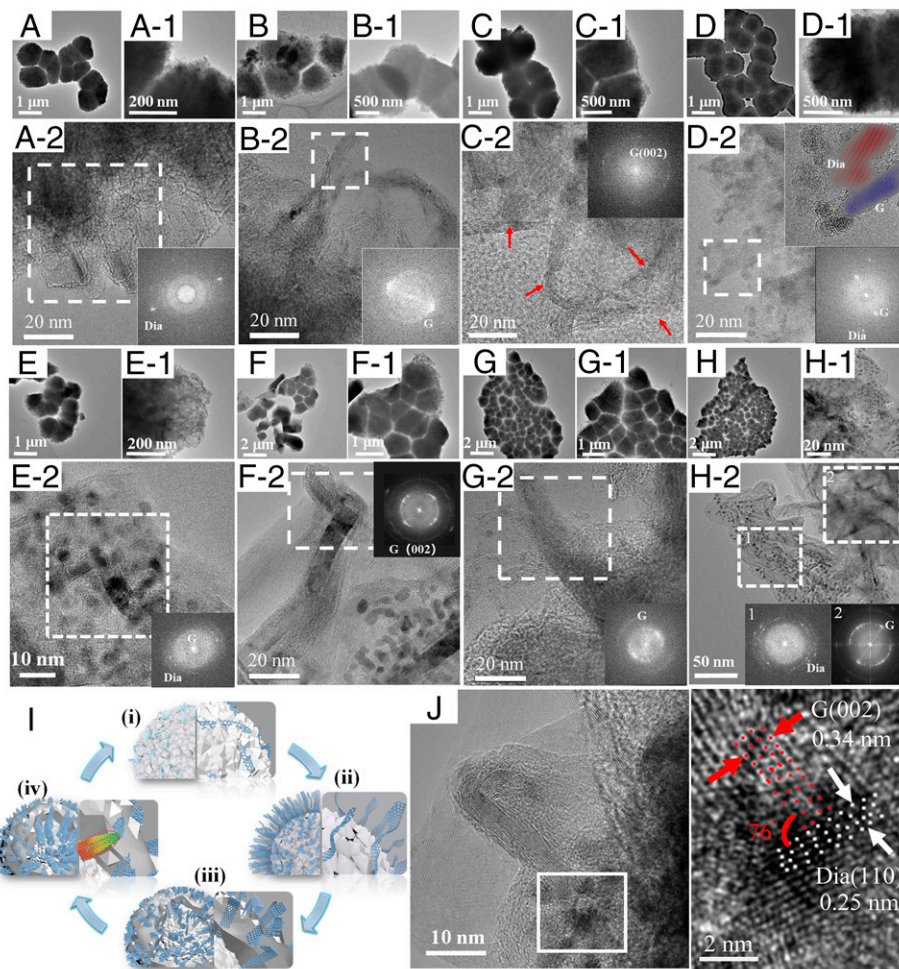**Fig. 2.** HRTEM images of samples growing (*A*)–(*A*-2) 0 s, (*B*)–(*B*-2) 30 s, (*C*)–(*C*-2) 60 s, (*D*)–(*D*-2) 90 s, (*E*)–(*E*-2) 120 s, (*F*)–(*F*-2) 150 s, (*G*)–(*G*-2) 180 s, and (*H*)–(*H*-2) 210 s during the second growth process at 1,800 W. All white-dotted-line boxes are the areas corresponding to the inset FFT images. The red arrows in (*C*-2) are used to mark the heads bending of graphene. (*I*) Sketch of the cyclical growth of the NCD film in the HFCVD process. (*J*) Shows the VGs with their roots in 30-s sample, and (*J*-1) shows the enlarged area of the white square in (*J*), indicating the graphite/diamond interface. The red and white arrows indicate the (002) plane of graphite and the (110) plane of diamond, respectively.

and 2,950 cm^{-1} decrease, indicating that the VGs disappear, NCD appears, and graphite becomes disordered. During 150 to 210 s, the change in Raman spectra is similar to that of 30 to 90 s, confirming that the periodic change observed in the surface morphology originates from the alternative appearance of VGs and NCD.

To understand this incredible periodicity evolving process, HRTEM measurements on the newly formed layer were performed (Fig. 2). The 0-s sample (Fig. 2*A*) displays large rod-like diamond crystals evidenced by diffraction spots from the diamond (111) orientation in the inset Fourier transform (FFT) image. For 30-s sample (Fig. 2*B*), a large number of long and flexible VGs appear with an interplanar spacing of 0.34 nm for the G (002) orientation in the inset fast (FFT). For the 60-s sample, VGs become straight with their heads bending marked by red arrows in Fig. 2*C*-2. After that, VGs disappear, and a number of straighter and thicker graphite nanorods appear in the 90-s sample (Fig. 2*D*-2). Additionally, a flake-like diamond crystal (red image in Fig. 2*D*-2) suggests that diamond begins to appear, in good agreement with the SEM and Raman spectra. For the 120-s sample, many nanodiamond crystals naked on the edge of cauliflower-like particles covered the graphite nanorods (Fig. 2*E*-2). These results confirm the NCD characteristics observed in the Raman spectrum. In the following growth, flexible VGs appear again in 150 s

(Fig. 2*F*), straight and thick VGs are observed in 180 s (Fig. 2*G*), and nanodiamond-rich district (area 1) is covered again on graphite rods (area 2) in 210 s (Fig. 2*H*), which repeats the growth process of 30 to 90 s and accords with the results of SEM and Raman spectra. Moreover, the clear interface between diamond (110) plane and flexible graphite (002) plane (Fig. 2*J* for 30-s sample and *SI Appendix*, Fig. S3 for 150-s sample) is found. The intersection angles are 76° for the 30-s sample and 89° for the 150-s sample, elaborating that the (002) graphite band directly grows upright on the surface of diamond with various patterns. This is quite different from the reported conclusion that the VGs were likely rooted on the amorphous carbon phases (29–31).

The above results reveal that the periodicity appearance of VGs and NCD in the CVD process (Fig. 2*I*) actually includes the following stages: NCD grains (i stage, samples 0-s and 120-s), the initial growth of small VGs (ii stage, samples 30-s and 150-s), large VGs (iii stage, samples 60-s and 180-s), graphite nanorods (iv stage, samples 90-s and 210-s), and returning to NCD grains (i stage). This phenomenon means that VGs transit to graphite nanorods as VGs disappear in the CVD process. Moreover, the FWHM value of the G band dramatically increases from 46.68 cm^{-1} of 60-s sample to 81.62 cm^{-1} (90-s sample) and 62.98 cm^{-1} (120-s sample), suggesting that graphite becomes more disordered. The appearance of diamond nanocrystals

indicates that the graphite probably transforms into diamond. Additionally, there are a number of graphite nanorods in samples 90-s, 120-s, and 210-s from HRTEM (Fig. 2 *D*-2, *E*-2, and *H*-2), while in the final NCD films (the 0-s sample), there are no residual graphite nanorods but large and rod-like diamond crystals, further evidencing that graphite transitions to diamond. In other words, diamond grains do not grow by carbon atoms piling up to form sp³ structures but are formed by phases transiting from graphite in CVD. These are very interesting phenomena and have never been observed before. To confirm our judgment, we designed a slower growth process by reducing the growth power to 1,600 W and extending the growth period to 12 min to capture clear transition evidence of diamond formation.

The surface and sectional Field emission scanning electron microscopy (FESEM) images (*SI Appendix,* Fig. S4) and Raman spectra (*SI Appendix,* Fig. S5) for the series samples express the same cyclical appearance and disappearance of VGs as those of samples growing under 1,800 W (Fig. 2*I*). Moreover, the growth cycle under 1,600 W is ~4 min, longer than ~90 s under 1,800 W, illustrating that a low growth power of 1,600 W indeed slows the growth speed and extends the growth cycle.

The microstructure of a 0-min sample is the same as that of a 0-s sample (Fig. 2), exhibiting large rod-like diamond crystals poke out from cauliflower-like particles. For growth times of 2, 6, and 10 min, in Fig. 3 *A*, *C*, and *E*, respectively, flexible VGs appear. For growth times of 4, 8, and 12 min, in Fig. 3 *B*, *D*, and *F*, respectively, VGs disappear. Specifically, for the 4-min sample, straight graphite is the main feature (Fig. 3*B*), while many graphite nanorods are observed in the 8-min sample (Fig. 3*D*). Interestingly, the inset FFT image (Fig. 3*D*) from the single graphite nanorod has both graphite [darker (002) diffraction spots] and diamond [bright (111) diffraction spots] compared with the 4-min sample. For the 12-min sample (Fig. 3*F*), the large diamond grains are the main composition, as evidenced by the inset FFT image of diamond (111) diffraction spots and the Raman spectrum in *SI Appendix,* Fig. S5, which is similar to that of the 0-min sample, confirming that the graphite has completely transformed into diamond and formed a bulk diamond crystal compared with the first (2 to 4 min) and second cycles (6 to 8 min). These results undoubtedly verify that the mixed appearance of diamond (111) and graphite (002) in the sample 8-min is a transitional period from graphite to diamond.
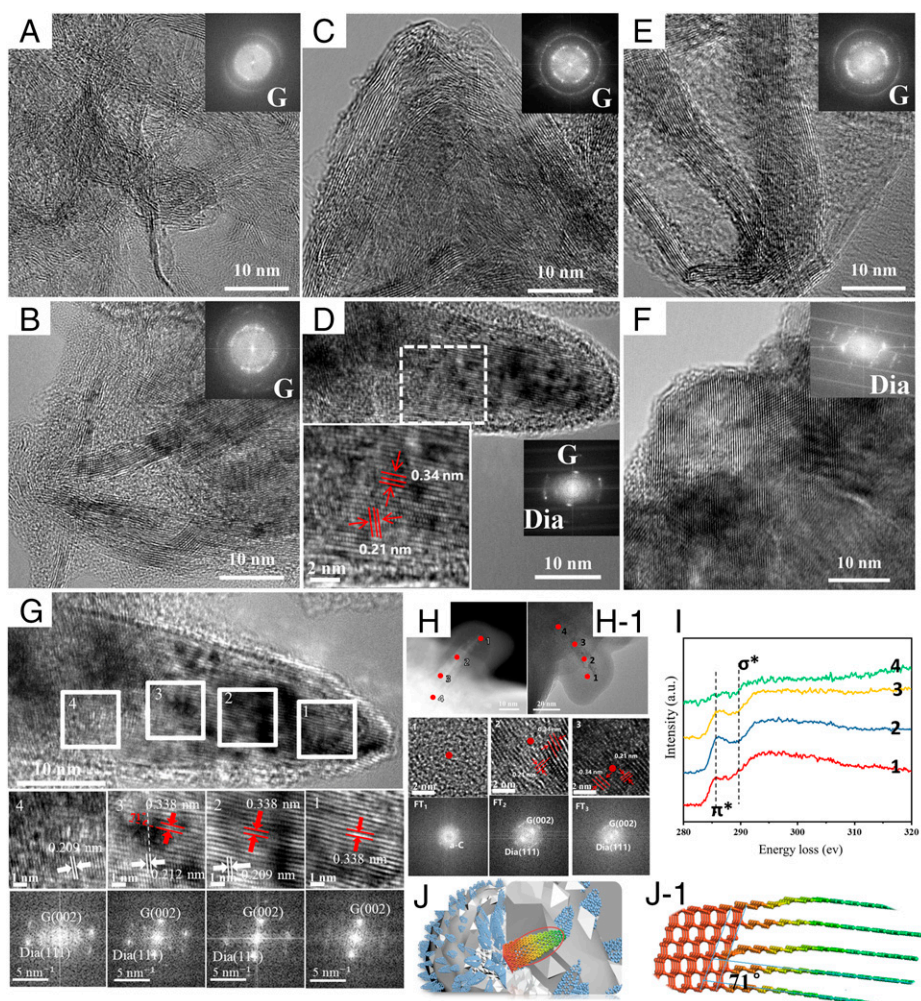

Fig. 3. TEM images for samples growing after (*A*) 2 min, (*B*) 4 min, (*C*) 6 min, (*D*) 8 min, (*E*) 10 min, and (*F*) 12 min in the second growth process with a power of 1,600 W. The white-dotted-line box in (D) is the area corresponding to the inset FFT image and the left inset enlarged image. The red arrows indicate the planes with the distance of 0.34 nm and 0.21 nm, respectively. Extensive analysis of the TEM images (G) of graphite needles in samples growing after 8 min in the second growing process at 1,600 W clearly exhibits the phase transformation process from graphite to diamond. The white boxes are the areas for the corresponding enlarged images and FFT images below, and the red and white arrows indicate the plane distance. (H) and (H-1) are the HADDF and bright field TEM images for another graphite needle, respectively, with the corresponding enlarged images and FFT images below. The EELS spectra (I) of the different sites marked by red points from another phase transforming needle shown in (H)/(H-1). (J)/(J-1) Sketch of the phase transformation from graphite to diamond in the graphite needle grown on cauliflower-like particles.

Fig. 3*G* displays the structural evolution in the 8-min sample with four typical areas selected from its head to root. In its head (part 1), FT1 shows the 0.34-nm interplanar spacing of the graphite (002) orientation. For center area 2 (FT2), a new and gloomy lattice plane (0.21 nm) overlaps on the graphite (002) lattice plane at an angle of 71 degrees, which agrees with that found in the graphite-diamond transition under high-pressure and high-temperature conditions (32, 33). This indicates that the lattice planes (0.21 nm) originating from diamond are derived from the graphite (002) plane by lattice distortion. For area 3 (FT3), diamond lattice planes (0.21 nm) become clearer as the graphite (002) lattice planes become indistinct, elaborating the strengthened diamond lattice planes (0.21 nm) and the weakened graphite (002) lattice planes. For area 4 (FT4), diamond lattice fringes (0.21 nm) become the main lattice with a near disappearance of graphite (002) lattice fringes, indicating that graphite completely transits to diamond.

Another graphite needle (Fig. 3*H*) with a transition intermediate state also confirms this phase transformation. Their located electron energy loss spectroscopy (EELS) analysis (Fig. 3*I*) shows that the intensity of the π^*-band (sp^2 carbon) gradually weakens from location 1 to 4, while that of the σ^*-band (sp^3 carbon) becomes stronger from location 2 to the root (location 4) of the nanorod. Additionally, the corresponding lattice distortion process from 0.32-nm lattice spacing to 0.21-nm lattice spacing is also shown below. Because site 4 is located inside the sample, it is too thick to detect its lattice. These results also indicate that diamond (111) with a lattice spacing of 0.21 nm appears, while graphite (002) with a lattice spacing of 0.32 nm disappears, suggesting that graphite transforms into diamond in the CVD process (Fig. 3 *J* and *J*-1). This is quite different from the generally accepted process involving the activation of a carbon-containing gas source into sp^2 or sp^3 species, and all of them graft on the dangling bonds on the vacancy to pile up to form diamond (34, 35).

It is well known that graphite can transit to diamond under high temperature and high pressure, while in our case, graphite transforms into diamond under low pressure, suggesting that there are other factors that help this transformation. X-ray photoelectron spectroscopy (XPS) (Fig. 4*A* and *SI Appendix,* Fig. S7) reveals obvious Ta and O characteristic absorption peaks, in which the oxygen atoms are bonded with carbon. Here, Ta comes from the tantalum hot filament in CVD. Furthermore, HAADF and energy dispersive spectrometry (EDS) mapping images (Fig. 4*B*) show atomically dispersed Ta atoms. This gives us inspiration to determine whether Ta atoms play a key role in the phase transition. To solve this problem, we constructed a model to simulate this transition (*SI Appendix,* Fig. S8). The results show that a single-side hydrogenated graphene layer transits into diamond, with the activation barrier decreasing from 0.82 eV/unit cell without Ta to −5.38 eV/unit cell after Ta is added (black and red lines in Fig. 4*C*), indicating that hydrogenated graphene can spontaneously transform into diamond after Ta is added. Considering the complex atomic components, including Ta, O, and H, in the hot filament growth environment, we also constructed a model (*SI Appendix,* Fig. S9*A*) of a double layer of graphene on the surface of oxygen-terminated diamond (111) to simulate the phase transition. Fig. 4*C* shows that the activation barrier of the O-terminated system without tantalum atoms is 0.48 eV/unit cell, while it sharply decreases to −3.99 eV/unit cell for the Ta-added O-terminated system. This suggests that O-terminated system adsorbed by Ta atoms can also spontaneously transform into diatomic layer diamond. The final structures of the O-terminated and H-terminated systems (Fig. 4*D*) and the bond length as well as bond angles

(*SI Appendix,* Table S2) show that the structure of the O-terminated system deviates more from the bulk diamond than that of the H-terminated system, leading to a slightly larger energy of the final structure for the O-terminated system. The differential charge diagrams of the key steps (0, 7, 8, and 9) (Fig. 4*E* and *SI Appendix,* Fig. S9) intuitively show that both Ta and O atoms contribute to the process of the graphene phase transforming into diamond. Moreover, in the CVD system without a source of Ta, hydrogen is the essential source for the growth of diamond. It was reported that as the graphene was hydrogenated with two sides, it spontaneously transformed to diamond with the activation barrier of ∼−5 eV/unit cell (36, 37), which is less than that of the single-side hydrogenated graphene system with Ta. This further suggests that Ta is of greater benefit to the graphite-diamond phase transformation than H atoms. As a conclusion, the phase transformation from graphite to diamond occurs under the special conditions, including two-side hydrogenated graphene layer, single-side hydrogenated graphene layer with Ta atoms, and single-side O-terminated system with Ta atoms. These factors are available for various CVD technologies, suggesting that diamond is formed by the phase transformation from graphite in CVD.

In summary, we observed the growth process of NCD films in hot filament chemical vapor deposition (HFCVD) by controlling the short-term growth to directly characterize the nanolayer on the cauliflower-like particles, exhibiting phase transition-induced diamond formation from graphite. This is quite different from the general knowledge that graphite is etched by hydrogen and that sp^3 carbon species pile up to form a diamond structure. The results show that the mixture of Ta, O, and H atoms allows graphite to spontaneously transform into diamond. This supplies a way to synthesize large-area diamond based on large-sized graphite under low pressure and provides an angle to understand the growth mechanism of materials with sp^2 and sp^3 electronic configurations during the CVD process.

Methods

Experimental. We designed a two-step process to exhibit the growth evolution, in which we first terminated the growth before the continuous film was formed and obtained SPF films. Then, we used these SPF films as the template to grow the films with short growth times, as shown in *SI Appendix,* Fig. S1, producing a surface with nanometer-scale thickness, which can be directly observed by using HRTEM without mechanical treatments. This protects the microstructure of the films growing under different times from damage, allowing us to observe the real growth process of the films.

Specifically, a two-step method was used to prepare the samples by using a commercial HFCVD system. The first step was growing SPF nanocrystalline diamond films on a silicon substrate under the same conditions for all samples. The Si wafer was continually polished by using diamond powders for 20 min and then rinsed by using deionized water and acetone. Pure hydrogen (99.999%) was used as the growth atmosphere and to pump acetone, which was the carbon source, into the reactor chamber. The flow rates for the hydrogen source and the carbon source were 200 sccm and 90 sccm, respectively. The pressure of the reactor chamber was 1,600 Pa, and the power of growth was 2,200 W (the voltage was ∼20 V, and the current was ∼120 A). The first growth process lasts for 20 min. Then, two series of samples are designed to control the growth process. The growth power of the first series is set as 1,800 W, and the growth time is set as 0, 30, 60, 90, 120, 180, and 210 s. The sample names are 0-s, 30-s, 60-s, 90-s, 120-s, 180-s, and 210-s, respectively. Another series of samples had a growth power of 1,600 W to further slow the growth rate and prolong the growth time to exhibit the growth process of the films. The growth time is set longer as 2, 4, 6, 8, 10, and 12 min, and the sample names are 2-min, 4-min, 6-min, 8-min, 10-min and 12-min, respectively. During these growth processes, the hydrogen source was turned off, and the carbon source was restored to 100
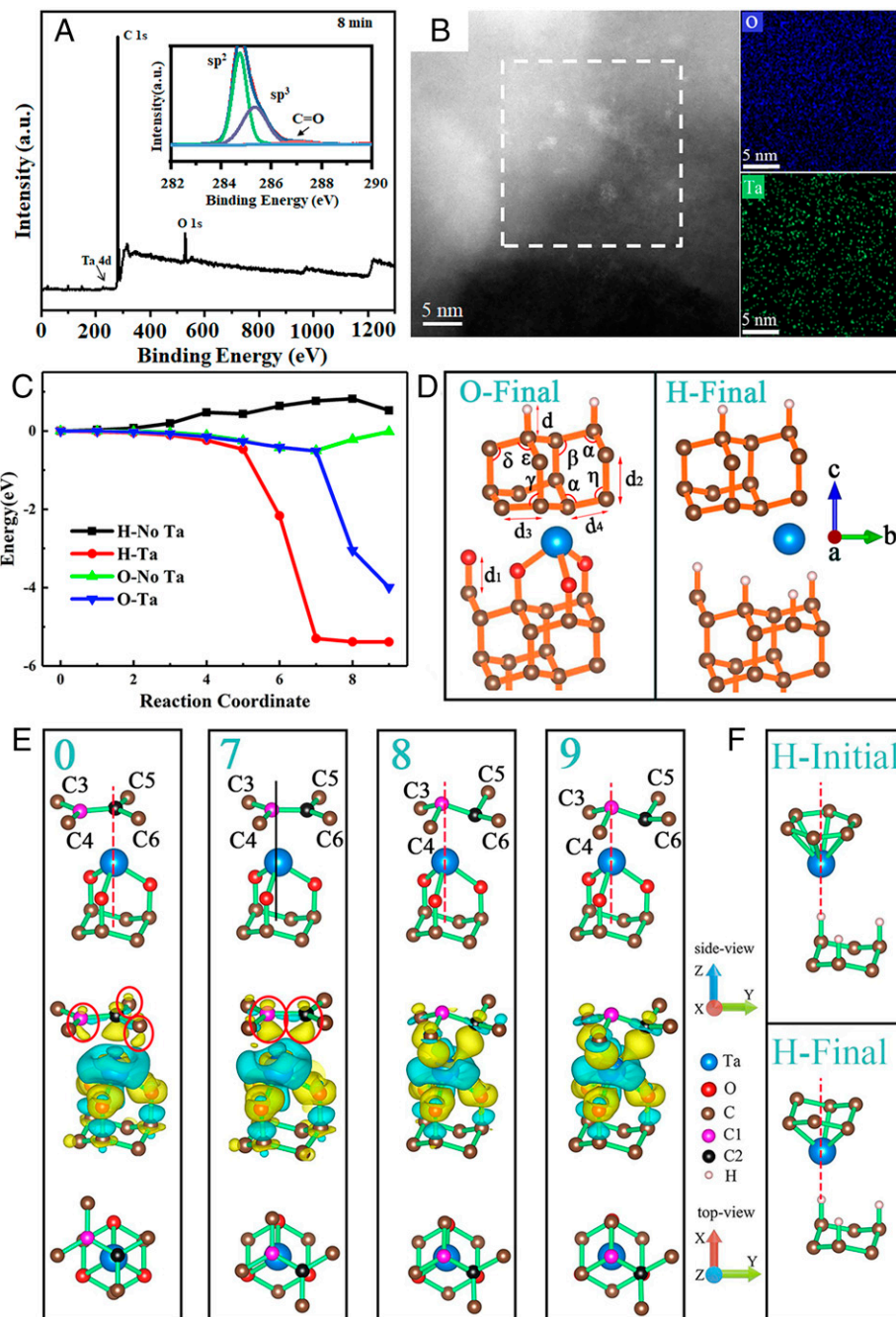
Fig. 4. (*A*) XPS spectrum and (*B*) Ta monoatomic dispersion image in the 8-min sample with the distribution mapping of O and Ta from the white-dotted-line box. (*C*) The calculated activation barrier from single-side hydrogenated graphene and O-terminated system to the diatomic diamond layer without Ta added and with Ta added. (*D*) The bond length and bond angle model of O-terminated and H-terminated final state structures with Ta. (*E*) Charge density differences for structure images 0, 7, 8, and 9 steps in *C*. (*F*) Charge density differences for the H-terminated structure. The yellow and light-blue regions represent electron accumulation and depletion, respectively. The surface values are 0.0034 e/Å^3.

sccm. After that, the growth power decreased to zero at a rate of 1 V/s with the closed carbon source.

Characterizations. FESEM (FEI Nano Nova 450) was used to observe the morphologies of the samples at a low voltage of 5 or 3 kV. To protect the microstructure of the NCD films from damage during TEM sample preparation, small fragments of film were scraped down from the silicon substrate and loaded on copper mesh. The submicroscopic structures or ultrastructures of the samples were characterized by using HRTEM (FEI Talos-s, 200 kV accelerator voltage) and aberration-corrected scanning transmission electron microscopy (Titan G2 80-200 ChemiSTEM). EDS and EELS were used to recognize the composition information of the samples. Raman spectra were taken to evaluate the structure and components of the films. A Labram high-resolution spectrometer (Horiba

Jobin-Yvon) interfaced with an Olympus microscope (objective 50×) was used to acquire the Raman spectra for four different sites, and the spectra were collected in the range of 500 to 3,500 cm^{-1}. Some of the spectra had been deconvoluted well into Gaussian lines.

Calculation Method. Total calculations are performed within the framework of density functional theory as implemented in the Vienna Ab initio Simulation Package (version 5.4.4) (38). The generalized gradient approximation of the Perdewe-Burkee-Ernzerhof exchange-correlation functional and projector augmented wave potentials were adopted to calculate all structure relaxations and electronic structure calculations (39). The cutoff energy was set to 520 eV with an energy precision of 10^{-4} eV, and a $4 \times 4 \times 1$ Monkhorst-Pack k-points grid for calculations was used to give a sufficient convergence of the total energies

during the structural relaxation. In all calculations, we guarantee that the vacuum space is at least 25 Å to reduce the interaction caused by periodic boundary conditions between adjacent layers. In the process of structural relaxation, the atoms in the bottom five layers of oxygen-terminated diamond are fixed, and the remaining atoms are relaxed. Based on the first-line principle, the transition barrier is calculated by using the nudge performance band method (40). This method works well by optimizing multiple intermediate images along the reaction path. The charge density difference $\Delta\rho$ is calculated by the formula $\Delta\rho = \rho_{Ta+surf+graphene} - \rho_{Ta} - \rho_{surf} - \rho_{graphene}$, where $\rho_{Ta+surf+graphene}$ is the charge density of the diamond surface with Ta atoms and two graphene layers, ρ_{Ta}, ρ_{surf}, and $\rho_{graphene}$ are the charge densities of isolated Ta atoms, the oxygen-terminated diamond surface, and two graphene layers, respectively.

1. C. Dang *et al.*, Achieving large uniform tensile elasticity in microfabricated diamond. *Science* **371**, 76–78 (2021).
2. P. Siyushev, *et al.*, Photoelectrical imaging and coherent spin-state readout of single nitrogen-vacancy centers in diamond. *Science* **363**, 728–731 (2019).
3. W. A. Yarbrough, R. J. Messier, Current issues and problems in the chemical vapor deposition of diamond. *Science* **247**, 688–696 (1990).
4. Y. Yue *et al.*, Hierarchically structured diamond composite with exceptional toughness. *Nature* **582**, 370–374 (2020).
5. B. S. Miller *et al.*, Spin-enhanced nanodiamond biosensing for ultrasensitive diagnostics. *Nature* **587**, 588–593 (2020).
6. W. G. Eversole, "Synthesis of diamond." US Patent 3 (1962).
7. S. Matsumoto, Y. Sato, M. Tsutsumi, N. J. Setaka, Growth of diamond particles from methane-hydrogen gas. *J. Mater. Sci.* **17**, 3106–3112 (1982).
8. S. T. Lee, Z. Lin, X. Jiang, CVD diamond films: Nucleation and growth. *Mater. Sci. Eng. R Rep.* **25**, 123–154 (1999).
9. S. T. Lee *et al.*, A nucleation site and mechanism leading to epitaxial growth of diamond films. *Science* **287**, 104–106 (2000).
10. Y. Lifshitz, T. Köhler, T. Frauenheim, I. Guzmann, A. Hoffman, *et al.*, The mechanism of diamond nucleation from energetic species. *Science* **297**, 1531–1533 (2002).
11. B. Sun, X. Zhang, Z. Lin, Growth mechanism and the order of appearance of diamond (111) and (100) facets. *Phys. Rev. B Condens. Matter* **47**, 9816–9824 (1993).
12. K. A. Feng, Z. D. Lin, Adsorption action of methylene CH_2 during diamond film growth on (100) surface by hot filament chemical vapor deposition (HFCVD). *J. Phys. Chem. Solids* **55**, 525–529 (1994).
13. X. Li, J. Perkins, R. Collazo, R. J. Nemanich, Z. Sitar, Investigation of the effect of the total pressure and methane concentration on the growth rate and quality of diamond thin films grown by MPCVD. *Diamond Related Materials* **15**, 1784–1788 (2006).
14. P. W. May, M. Ashfold, Y. A. Mankelevich, Microcrystalline, nanocrystalline, and ultrananocrystalline diamond chemical vapor deposition: Experiment and modeling of the factors controlling growth rate, nucleation, and crystal size. *J. Appl. Phys.* **101**, 473 (2007).
15. M. N. R. Ashfold, P. W. May, J. R. Petherbridge, K. N. Rosser, N. V. Suetinb, Unravelling aspects of the gas phase chemistry involved in diamond chemical vapour deposition. *Phys. Chem. Chem. Phys.* **3**, 3471–3485 (2001).
16. A. Tallaire *et al.*, Multiple growth and characterization of thick diamond single crystals using chemical vapour deposition working in pulsed mode. *J. Cryst. Growth* **291**, 533–539 (2006).
17. L. Schafer, C. P. Klages, U. Meier, K. Kohse-Hinghaus, Atomic hydrogen concentration profiles at filaments used for chemical vapor deposition of diamond. *Appl. Phys. Lett.* **58**, 571 (1991).
18. F. G. Celii, J. E. Butler, Hydrogen atom detection in the filament-assisted diamond deposition environment. *Appl. Phys. Lett.* **54**, 1031–1033 (1989).
19. S. J. Harris, A. M. Weiner, T. A. Perry, Measurement of stable species present during filament-assisted diamond growth. *Appl. Phys. Lett.* **53**, 1605–1607 (1988).
20. L. B. Zhao, K. A. Feng, Z. D. Lin, The formation of atomic steps in chemical vapour deposition diamond growth. *Diamond Relat. Mater.* **3**, 155–159 (1994).
21. T. R. Anthony, Metastable synthesis of diamond. *Vacuum* **41**, 1356–1359 (1990).
22. X. Jiang, W. J. Zhang, M. Paul, C. P. Klages, Diamond film orientation by ion bombardment during deposition. *Appl. Phys. Lett.* **68**, 1927–1929 (1996).
23. W. J. Zhang, X. Jiang, The growth characteristics of (001) oriented diamond layers on (111) diamond face via bias-assisted chemical vapor deposition. *Appl. Phys. Lett.* **68**, 2195–2197 (1996).
24. W. J. Zhang, X. Jiang, Y. B. Xia, The selective etching with H^+ ions and its effect on the oriented growth of diamond films. *J. Appl. Phys.* **82**, 1896–1899 (1997).
25. X. J. Hu, "A separated particles formed nanocrystalline diamond film and its preparation method." CN201510149374.4 (2015).
26. H. Kuzmany, R. Pfeiffer, N. Salk, B. Günther, The mystery of the 1140 cm^{-1} Raman line in nanocrystalline diamond films. *Carbon* **42**, 911–917 (2004).
27. Z. Ni, Y. Wang, T. Yu, Z. Shen, Raman spectroscopy and imaging of graphene. *Nano Res.* **1**, 273–291 (2008).
28. A. C. Ferrari, D. M. Basko, Raman spectroscopy as a versatile tool for studying the properties of graphene. *Nat. Nanotechnol.* **8**, 235–246 (2013).
29 Y. Qi, B. Deng, X. Guo, S. Chen, J. Gao, *et al.*, Switching vertical to horizontal graphene growth using faraday cage-assisted PECVD approach for high-performance transparent heating device. *Adv. Mater.* **30**, 1704839 (2018).
30. J. K. Park, H. Kang, J. H. Kim, W. Choi, Improvement of electrical properties of carbon nanowall by the deposition of thin film. *J. Nanosci. Nanotechnol.* **18**, 6026–6028 (2018).
31. I. S. Hosu *et al.*, Carbon nanowalls: A new versatile graphene based interface for the laser desorption/ionization-mass spectrometry detection of small compounds in real samples. *Nanoscale* **9**, 9701–9715 (2017).
32. S. C. Zhu, X. Z. Yan, J. Liu, A. R. Oganov, Q. Zhu, A revisited mechanism of the graphite-to-diamond transition at high temperature. *Matter* **3**, 864–878 (2020).
33. W. R. L. Lambrecht *et al.*, Diamond nucleation by hydrogenation of the edges of graphitic precursors. *Nature* **364**, 607–610 (1993).
34. H. Liu, D. S. Dandy, Studies on nucleation process in diamond CVD: An overview of recent developments. *Diamond Relat. Mater.* **4**, 1173–1188 (1995).
35. J. E. Butler, Y. A. Mankelevich, A. Cheesman, J. Ma, M. N. R. Ashfold, Understanding the chemical vapor deposition of diamond: Recent progress. *J. Phys. Condens. Matter* **21**, 364201 (2009).
36. A. G. Kvashnin, L. A. Chernozatonskii, B. I. Yakobson, *et al.*, Phase diagram of quasi-two-dimensional carbon, from graphene to diamond. *Nano Lett.* **14**, 676–681 (2014).
37. L. Y. Antipina, P. B. Sorokin, Converting chemically functionalized few-layer graphene to diamond films: A computational study. *J. Phys. Chem. C* **119**, 2828–2836 (2015).
38. G. Kresse, J. Furthmüller, Efficient iterative schemes for ab initio total-energy calculations using a plane-wave basis set. *Phys. Rev. B* **54**, 11169–11186 (1996).
39. J. P. Perdew, K. Burke, M. Ernzerhof, Generalized gradient approximation made simple. *Phys. Rev. Lett.* **77**, 3865–3868 (1996).
40. G. Henkelman, B. P. Uberuaga, H. Jónsson, A climbing image nudged elastic band method for finding saddle points and minimum energy paths. *J. Chem. Phys.* **113**, 9901–9904 (2000).